


Photoelectrochemistry Hot Paper

 How to cite: *Angew. Chem. Int. Ed.* **2021**, *60*, 23651–23655

International Edition: doi.org/10.1002/anie.202108994

German Edition: doi.org/10.1002/ange.202108994

Identifying Reactive Sites and Surface Traps in Chalcopyrite Photocathodes

Yongpeng Liu, Maria Bouri, Liang Yao, Meng Xia, Mounir Mensi, Michael Grätzel, Kevin Sivula,* Ulrich Aschauer,* and Néstor Guijarro*

Abstract: Gathering information on the atomic nature of reactive sites and trap states is key to fine tuning catalysis and suppressing deleterious surface voltage losses in photoelectrochemical technologies. Here, spectroelectrochemical and computational methods were combined to investigate a model photocathode from the promising chalcopyrite family: $\text{CuIn}_{0.3}\text{Ga}_{0.7}\text{S}_2$. We found that voltage losses are linked to traps induced by surface Ga and In vacancies, whereas operando Raman spectroscopy revealed that catalysis occurred at Ga, In, and S sites. This study allows establishing a bridge between the chalcopyrite's performance and its surface's chemistry, where avoiding formation of Ga and In vacancies is crucial for achieving high activity.

Understanding the atomic nature of reactive sites and surface traps is a key enabling step towards optimizing chemical conversion at semiconductor–liquid junctions.^[1–3] The recent development of operando analysis tools has provided deep insights into the operation of specific semiconductor electrodes for solar-driven H_2 production via water splitting.^[4–7] However, each material brings a unique atomic and electronic structure that requires the development of specific analysis tools and interpretation. One class of materials that offers a particular challenge is the chalcopyrites $\text{Cu}(\text{In,Ga})(\text{S,Se})_2$. These materials are gaining momentum as

prospective photocathodes for H_2 production in photoelectrochemical (PEC) water splitting cells.^[8–12] Their attractiveness relies on their superb optoelectronic properties, their compatibility with solution-based manufacturing techniques, their ready-to-market photovoltaic performance, and their well-positioned energy bands to trigger the hydrogen evolution reaction (HER), among others.^[13–15] While typical chalcopyrite photocathodes utilize a complex buried junction architecture,^[15,16] recently, a direct chalcopyrite/electrolyte interface has shown hours-stable H_2 -related saturation photocurrents close to the theoretical limit based on their band gap.^[13,14] While promising, given the multi-atomic surface of chalcopyrites, the origin of the surface reactivity remains to be elucidated, and moreover, an explanation for the inferior turn-on voltages (V_{on}) exhibited by these bare chalcopyrites is still missing. Therefore, a deeper understanding of the processes that govern V_{on} , such as the surface recombination and catalysis, is urgently needed to guide the optimization of bare chalcopyrites. For this purpose, here, we deployed an assortment of spectroelectrochemical and computational methods which provide new insights into the atomic nature of the reactive sites and trap states on the surface of a model chalcopyrite $\text{CuIn}_{0.3}\text{Ga}_{0.7}\text{S}_2$ (CIGS).

CIGS photocathodes were fabricated by sulfurizing nanocrystalline films as reported elsewhere.^[10] A complete characterization of the morphology, composition, and crystalline structure can be found in Figures S1–S3. The linear sweep voltammogram (LSV) of the CIGS film was recorded to assess the PEC response towards H_2 production (Figure 1 a). V_{on} is at ca. 0.1 V vs. RHE from where the photocurrent steadily increases up to 7 mA cm^{-2} at -0.4 V vs. RHE . The photocurrent was monitored to be stable over 150 h (Figure S4) under continuous operation showing no evidence of degradation, while the Faradaic efficiency of ca. 97% (Figures S5, S6) confirmed H_2 production and ruled out corrosion reactions.

Electrochemical impedance spectroscopy (EIS) was employed to explore the interfacial electronic structure under operation. The Mott–Schottky (M–S) plot (Figure 1 a) revealed that the flat band potential (V_{fb}) was located at 0.65 V vs. RHE, i.e., 550 mV more positive than V_{on} . This late onset could be explained by either Fermi level pinning (FLP) or a large overpotential for the reaction. The analysis under illumination allowed the extraction of the density of surface states (DOSS), a proxy for the charge accumulated at the interface under operation, which appeared at the photocurrent onset (Figure 1 a). This electronic signature, although not previously reported for HER photocathodes, has often been detected in photoanodes under water oxidation con-

[*] Y. Liu, Dr. L. Yao, M. Xia, Dr. M. Mensi, Prof. M. Grätzel,

Prof. K. Sivula, Dr. N. Guijarro

Institute of Chemical Sciences and Engineering

École Polytechnique Fédérale de Lausanne (EPFL)

Station 6, Lausanne 1015 (Switzerland)

E-mail: kevin.sivula@epfl.ch

nestor.guijarro@epfl.ch

Dr. M. Bouri, Prof. U. Aschauer

Department of Chemistry and Biochemistry

University of Bern

Freiestrasse 3, CH-3012 Bern (Switzerland)


E-mail: ulrich.aschauer@dcb.unibe.ch


Dr. N. Guijarro

Present address: Institute of Electrochemistry

Universidad de Alicante

Apartat 99, E-03080 Alacant (Spain)

 Supporting information and the ORCID identification number(s) for

 the author(s) of this article can be found under:

<https://doi.org/10.1002/anie.202108994>


© 2021 The Authors. *Angewandte Chemie International Edition* published by Wiley-VCH GmbH. This is an open access article under the terms of the Creative Commons Attribution Non-Commercial License, which permits use, distribution and reproduction in any medium, provided the original work is properly cited and is not used for commercial purposes.

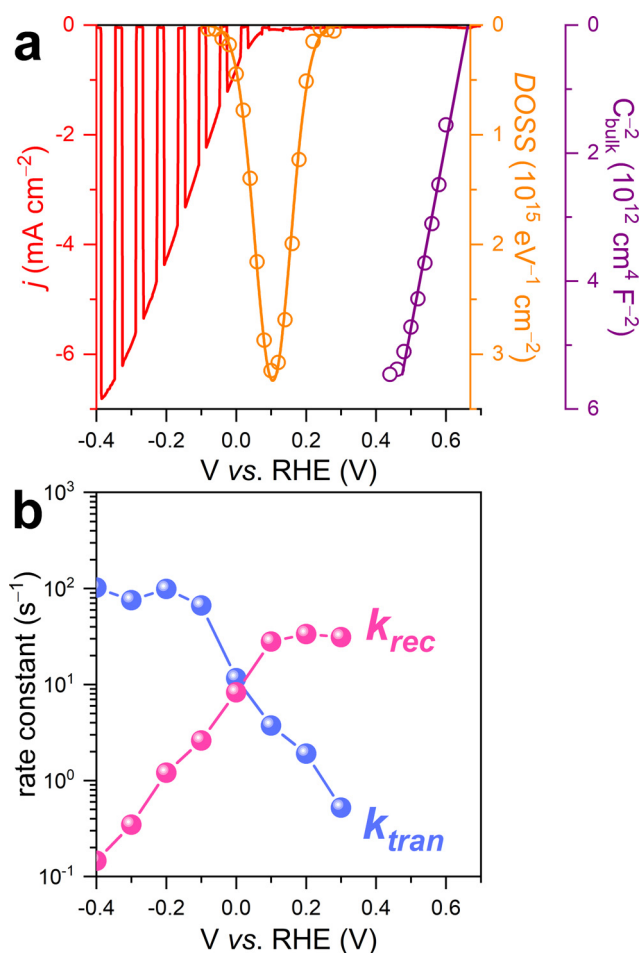


Figure 1. a) LSV of CIGS photocathode measured at intermittent simulated 1 sun condition in pH 6.1 buffer solution. Energetic distribution of DOSS with the corresponding Gaussian fit. The M–S plot with linear regression. b) Pseudo first order rate constants for charge transfer k_{tran} and surface recombination k_{rec} as a function of the applied potential.

ditions and was interpreted as the build-up of intermediate species at the interface when the catalytic reaction takes place.^[17–20] It is plausible to consider that this surface charging is linked to the adsorption of atomic hydrogen, which precedes the hydrogen evolution.

To find the origin of the voltage bottleneck, we decouple the surface recombination and reaction dynamics at the CIGS/electrolyte interface by means of intensity-modulated photocurrent spectroscopy (IMPS).^[21] Figure 1b depicts the evolution of the rate constants for charge transfer (k_{tran}) and surface recombination (k_{rec}) as a function of the applied potential. At low applied bias (> 0.1 V vs. RHE), k_{tran} steadily increased whereas k_{rec} remained constant. This is a common sign of FLP (Figure S7).^[22] Note that coupling a state-of-the-art Pt HER electrocatalyst barely impinged V_{on} supporting that voltage losses were primarily governed by FLP (Figure S8).^[23] At high applied bias (< 0.1 V vs. RHE), the behavior of the rate constants reversed, i.e., k_{tran} appeared to be constant while k_{rec} steadily dropped with more negative potentials. This is the expected response when a band-edge

pinning regime dominates (Figure S7). Note that an extended M–S analysis corroborated the occurrence of FLP both in dark and under illumination (SI Section S11.2). Although these results confirmed the FLP as the main responsible for the voltage bottleneck, the energy and the chemical nature of the surface traps behind the FLP remain to be identified.

Photoluminescence (PL) spectroscopy has been successfully exploited to detect surface energy traps.^[24,25] Figure 2a depicts the PL spectrum of the CIGS. The sharp band at ca. 590 nm was assigned to the band-edge emission, which matches with the $E_{\text{g}} = 2.0$ eV estimated from the incident photon-to-current efficiency spectrum (Figure S9). The broad band at longer wavelengths could be attributed to radiative processes involving trap states. Two Gaussian curves centered at 783 nm and 641 nm were required to fit this band, evidencing the presence of at least two emission centers. Several studies have ascribed this signal to the transition from the conduction band edge (E_{CB}) to shallow acceptor levels that lie near the valence band edge (E_{VB}).^[24,26,27] Figure 2c shows an estimate of the energy band positions including the location of the traps.^[28] Figures 2a,b displays the PL spectrum in terms of potential for the sake of comparison with LSVs (Figure S10). The photocurrent remains negligible until the applied potential surpasses the traps, validating the hypoth-

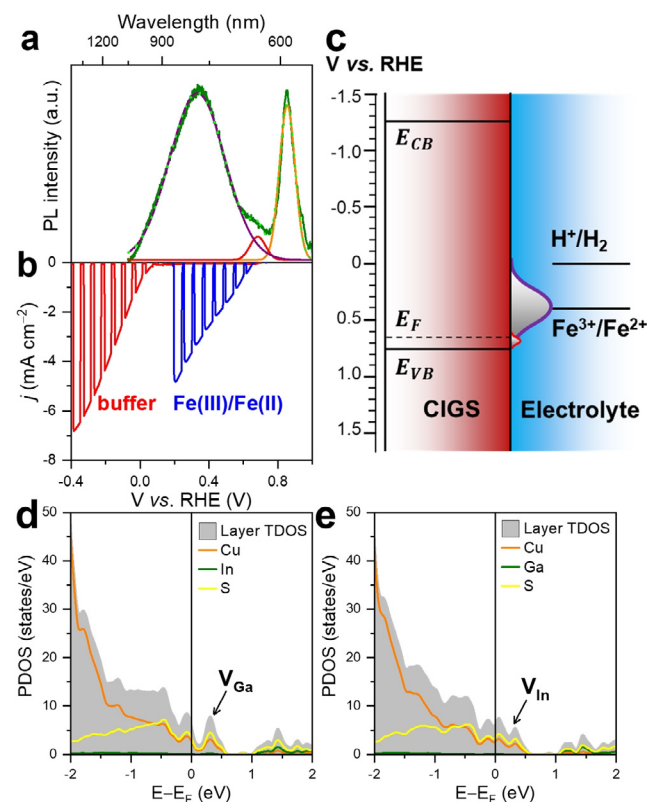


Figure 2. a) PL spectrum (green solid line), including the corresponding Gaussian fitting curves assigned to trap states (blue and red) and band-edge emission (orange), and the envelope/fitting curve (green dashed line). b) LSV of the CIGS photocathode measured under intermittent simulated 1 sun illumination in pH 6.1 buffer solution and in 0.5 M $\text{Fe}^{\text{III}}/\text{Fe}^{\text{II}}$. c) Schematic band diagram of CIGS at V_{b} . PDOS of a CIGS (112) surface with surface d) Ga and e) In vacancies.

esis that performance is governed by FLP. To narrow down the energy location of the traps, we tested the PEC response in the presence of the $[\text{Fe}(\text{CN})_6]^{3-}/[\text{Fe}(\text{CN})_6]^{4-}$ redox couple, denoted as $\text{Fe}^{\text{III}}/\text{Fe}^{\text{II}}$. We hypothesized that an outer-sphere redox couple located near the traps would allow to circumvent the voltage bottleneck by scavenging the trapped electrons. Indeed, the presence of $\text{Fe}^{\text{III}}/\text{Fe}^{\text{II}}$ triggered a rapid rise of the photocurrent from V_{ib} onwards with near-zero voltage losses. Nanoscale imaging of the surface photovoltage (SPV) was employed to elucidate the spatial distribution of the traps (Figure S13). The constant value of the SPV throughout the surface suggests that the traps are likely related to the surface's composition rather than to localized crystallographic defects such as grain boundaries or step edges.

To gain insight into the chemical identity of the traps, the projected density of states (PDOS) of few-layers-thick slab models of CIGS was computed examining the effect of intentionally introduced compositional defects (SI Section S13). Results in Figures 2d,e and S16 suggested that the presence of surface Ga (V_{Ga}) and In (V_{In}) vacancies caused the appearance of shallow acceptor levels that match well with those revealed by the PL and could act as trap states. Several studies support these findings.^[24,27,29] We speculate that the broad PL band could originate from these two types of vacancies.

We next explored the atomic nature of the reactive sites which, despite being crucial for optimizing the HER, remains overlooked in these materials, by implementing operando Raman spectroscopy. As sketched in Figure 3a, the three-electrode setup enables changing the applied potential on the CIGS electrode, while the excitation beam simultaneously initiates the PEC process and allows to collect the Raman spectra of the reactive interface. As shown in Figure 3b, small applied biases (> 0 V vs. RHE) delivered featureless spectra.

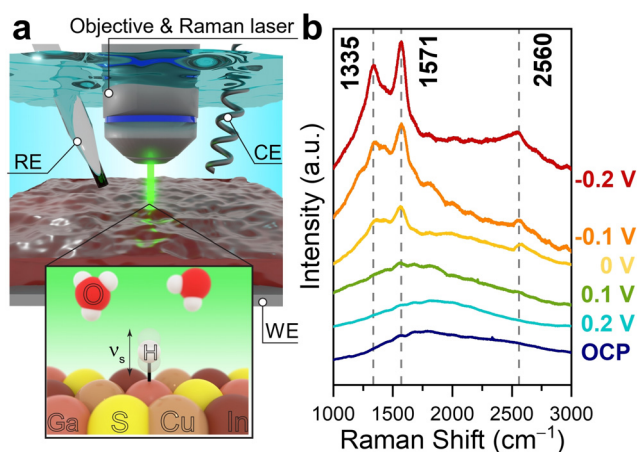


Figure 3. a) Schematic of operando Raman spectroscopy setup, including a portrait of the reaction intermediate: a hydrogen atom bound to the catalytic center (ν_s : characteristic stretching vibration of the bond). WE, CE, and RE represent the working, counter, and reference electrode, respectively. b) Raman spectra recorded at different applied potentials. OCP (navy line) refers to the spectrum recorded under open circuit conditions. A lower-Raman-shift spectra can be found in Figure S18.

However, higher applied bias (< 0 V vs. RHE) led to the appearance of three distinct peaks centered at 1335 cm^{-1} , 1571 cm^{-1} , and 2560 cm^{-1} , whose intensity increased with potential and photocurrent. Therefore, it is reasonable to link them to intermediate species involved in the PEC reaction. Note that bubbles were detected at the laser spot, supporting H_2 generation (Figure S17). The peaks were assigned, with caution, to the In–H, Ga–H and S–H vibration, on the basis of simulations and literature references (Table S1). While this result hinted at the participation of In, Ga, and S in the HER, the absence of a Cu–H vibration suggested that Cu did not take part in this reaction. We cannot discount Cu states involved in the HER via a fast kinetic reaction, which would render a low enough steady state concentration of Cu–H to be detected. The chemical states of the reactive interface were characterized by XPS before and after testing. We hypothesized that the oxidation state of the reactive sites could undergo partial reduction due to the electron accumulation and electron current preferentially flowing through them.^[30] The analyses revealed that while the Cu 2p spectra remained virtually unaltered, the In 3d, Ga 2p, and S 2p spectra changed during the reaction (Figure S20). The detected low-binding-energy contribution reflects an increased electron density in the surroundings of these ions that can be linked to their participation in the HER (SI Section S17).

With experimental evidence on the catalytic sites set in place, density functional theory calculations were undertaken to simulate the surface chemistry and establish a framework for interpretation (SI Section S13). The Gibbs free energy of atomic hydrogen bonding to the reactive site (ΔG_{H}) is considered a descriptor for the HER.^[31] Figure 4 depicts ΔG_{H} computed for the different adsorption sites available at the CIGS surface in two representative scenarios.^[32] Firstly, Figure 4a displays ΔG_{H} for single adsorption sites, somewhat corresponding to a low surface coverage of atomic hydrogen. The lowest ΔG_{H} estimated for Ga and In sites suggests that these are the preferential catalytic sites, while the weak adsorption (high ΔG_{H}) predicted for Cu accounts for its minor participation in the HER. Note that Cu orbitals barely contribute to the conduction band.^[33,34] In this light, the participation of these sites to PEC HER can be considered unlikely. However, Cu surface concentration plays a major role at defining the p-type behavior as well as the optoelec-

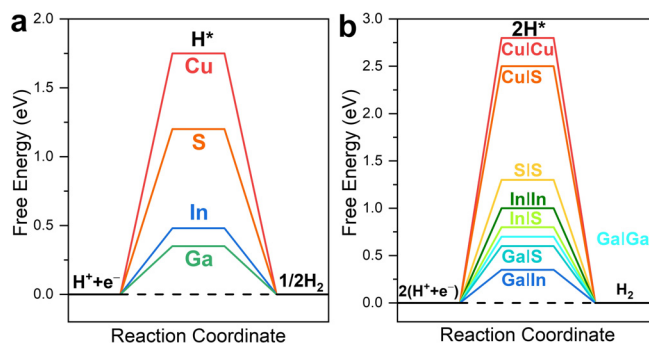


Figure 4. Computed free energy diagram for hydrogen evolution considering one (a) or two neighboring adsorption sites (b); H^* denotes the adsorbed hydrogen atom.

tronic properties of chalcopyrites.^[24,33,35] Secondly, ΔG_{H} was calculated assuming that adsorption occurs at two sites within minimal distance from each other on our model surface to simulate a high surface coverage situation. Here, Ga and In sites appeared as the preferred adsorption sites. Note that while isolated S was not active for HER (high ΔG_{H}), the proximity to Ga reduces ΔG_{H} , activating this site for the reaction and demonstrating that the adsorption characteristics are greatly influenced by the chemical environment.

In conclusion, the origin of the photovoltage bottleneck and catalytic properties of chalcopyrites using a CIGS photocathode was inspected. EIS and IMPS revealed that voltage losses were caused by the FLP existing near the V_{fb} . This was found to originate from traps attributed to V_{Ga} and V_{In} , according to computational simulations. Operando Raman spectroscopy identified Ga, In, and S as catalytic sites for HER, which is in good agreement with the activity predicted on the basis of ΔG_{H} . Note that the latter was estimated for a single configuration and expanding into other In/Ga or defective configurations could reveal the structure–catalysis relationship. These findings correlate the PEC response to the chemical nature of the interface providing guidelines for engineering the performance of chalcopyrites. It seems crucial to avoid the formation of V_{Ga} and V_{In} to suppress FLP and retain a high density of states.

Acknowledgements

This work was supported by the Swiss National Science Foundation (SNSF) under the Ambizione Energy grant (PZENP2_166871) and by the Gaznat-EPFL Research Program. M.B. and U.A. were supported by the Swiss National Science Foundation Professorship Grants PP00P2_157615 and PP00P2_187185. Calculations were performed on UBELIX, the HPC cluster at the University of Bern. M.X. is grateful for the support from the China Scholarship Council (No. CSC201806160172) and the Strategic Japanese–Swiss Science and Technology program (514259). The authors thank Harald Holze, Dr. Florian Le Formal and Dr. Florent Boudoire for setting up the light modulation methodologies and for the advice during data fitting. The authors thank Dr. Dan Ren for the helpful discussions. Open access funding provided by Ecole Polytechnique Federale de Lausanne.

Conflict of Interest

The authors declare no conflict of interest.

Keywords: chalcopyrite · density functional theory · photoelectrochemistry · spectroelectrochemistry · water splitting

- [1] H. Li, T. Wang, S. Liu, Z. Luo, L. Li, H. Wang, Z.-J. Zhao, J. Gong, *Angew. Chem. Int. Ed.* **2021**, *60*, 4034–4037; *Angew. Chem.* **2021**, *133*, 4080–4083.
- [2] B. Zhang, X. Huang, Y. Zhang, G. Lu, L. Chou, Y. Bi, *Angew. Chem. Int. Ed.* **2020**, *59*, 18990–18995; *Angew. Chem.* **2020**, *132*, 19152–19157.
- [3] X. Ning, P. Du, Z. Han, J. Chen, X. Lu, *Angew. Chem. Int. Ed.* **2021**, *60*, 3504–3509; *Angew. Chem.* **2021**, *133*, 3546–3551.
- [4] W. Yang, T. Moehl, E. Service, S. D. Tilley, *Adv. Energy Mater.* **2021**, *11*, 2003569.
- [5] E. Pastor, F. Le Formal, M. T. Mayer, S. D. Tilley, L. Francàs, C. A. Mesa, M. Grätzel, J. R. Durrant, *Nat. Commun.* **2017**, *8*, 14280.
- [6] F. Boudoire, Y. Liu, F. Le Formal, N. Guijarro, C. R. Lhermitte, K. Sivula, *J. Phys. Chem. C* **2021**, *125*, 10883–10890.
- [7] L. Yao, N. Guijarro, F. Boudoire, Y. Liu, A. Rahmanudin, R. A. Wells, A. Sekar, H.-H. Cho, J.-H. Yum, F. Le Formal, K. Sivula, *J. Am. Chem. Soc.* **2020**, *142*, 7795–7802.
- [8] S. Y. Chae, S. J. Park, S. G. Han, H. Jung, C.-W. Kim, C. Jeong, O.-S. Joo, B. K. Min, Y. J. Hwang, *J. Am. Chem. Soc.* **2016**, *138*, 15673–15681.
- [9] M. Moriya, T. Minegishi, H. Kumagai, M. Katayama, J. Kubota, K. Domen, *J. Am. Chem. Soc.* **2013**, *135*, 3733–3735.
- [10] N. Guijarro, M. S. Prévot, X. Yu, X. A. Jeanbourquin, P. Borno, W. Bourée, M. Johnson, F. Le Formal, K. Sivula, *Adv. Energy Mater.* **2016**, *6*, 1501949.
- [11] N. Gaillard, D. Prasher, M. Chong, A. Deangelis, K. Horsley, H. A. Ishii, J. P. Bradley, J. Varley, T. Ogitsu, *ACS Appl. Energy Mater.* **2019**, *2*, 5515–5524.
- [12] N. Guijarro, M. S. Prévot, M. Johnson, X. Yu, W. S. Bourée, X. A. Jeanbourquin, P. Borno, F. L. Formal, K. Sivula, *J. Phys. D* **2017**, *50*, 044003.
- [13] B. Mahmoudi, F. Caddeo, T. Lindenberg, T. Schneider, T. Hölscher, R. Scheer, A. W. Maijenburg, *Electrochim. Acta* **2021**, *367*, 137183.
- [14] C. P. Muzzillo, W. E. Klein, Z. Li, A. D. DeAngelis, K. Horsley, K. Zhu, N. Gaillard, *ACS Appl. Mater. Interfaces* **2018**, *10*, 19573–19579.
- [15] H. Kobayashi, N. Sato, M. Orita, Y. Kuang, H. Kaneko, T. Minegishi, T. Yamada, K. Domen, *Energy Environ. Sci.* **2018**, *11*, 3003–3009.
- [16] H. Kumagai, T. Minegishi, N. Sato, T. Yamada, J. Kubota, K. Domen, *J. Mater. Chem. A* **2015**, *3*, 8300–8307.
- [17] Y. Liu, F. L. Formal, F. Boudoire, L. Yao, K. Sivula, N. Guijarro, *J. Mater. Chem. A* **2019**, *7*, 1669–1677.
- [18] Y. Liu, M. Xia, L. Yao, M. Mendi, D. Ren, M. Grätzel, K. Sivula, N. Guijarro, *Adv. Funct. Mater.* **2021**, *31*, 2010081.
- [19] B. Klahr, S. Gimenez, F. Fabregat-Santiago, J. Bisquert, T. W. Hamann, *J. Am. Chem. Soc.* **2012**, *134*, 16693–16700.
- [20] B. Klahr, S. Gimenez, F. Fabregat-Santiago, T. Hamann, J. Bisquert, *J. Am. Chem. Soc.* **2012**, *134*, 4294–4302.
- [21] Y. Liu, F. Le Formal, F. Boudoire, N. Guijarro, *ACS Appl. Energy Mater.* **2019**, *2*, 6825–6833.
- [22] C. Zachäus, F. F. Abdi, L. M. Peter, R. van de Krol, *Chem. Sci.* **2017**, *8*, 3712–3719.
- [23] B. Kim, G.-S. Park, S. Y. Chae, M. K. Kim, H.-S. Oh, Y. J. Hwang, W. Kim, B. K. Min, *Sci. Rep.* **2018**, *8*, 5182.
- [24] J. H. Schön, E. Bucher, *Phys. Status Solidi A* **1999**, *171*, 511–519.
- [25] J. R. Botha, M. S. Branch, A. W. R. Leitch, J. Weber, *Phys. B* **2003**, *340–342*, 923–927.
- [26] C. Spindler, F. Babbe, M. H. Wolter, F. Ehré, K. Santhosh, P. Hilgert, F. Werner, S. Siebentritt, *Phys. Rev. Mater.* **2019**, *3*, 090302.
- [27] D. Colombara, H. Elanzeery, N. Nicoara, D. Sharma, M. Claro, T. Schwarz, A. Koprek, M. H. Wolter, M. Melchiorre, M. Sood, N. Valle, O. Bondarchuk, F. Babbe, C. Spindler, O. Cojocaru-Miredin, D. Raabe, P. J. Dale, S. Sadewasser, S. Siebentritt, *Nat. Commun.* **2020**, *11*, 3634.
- [28] J. Fu, F. Wang, Y. Xiao, Y. Yao, C. Feng, L. Chang, C.-M. Jiang, V. F. Kunzelmann, Z. M. Wang, A. O. Govorov, I. D. Sharp, Y. Li, *ACS Catal.* **2020**, *10*, 10316–10324.
- [29] S.-H. Wei, S. B. Zhang, A. Zunger, *Appl. Phys. Lett.* **1998**, *72*, 3199–3201.

- [30] Z. M. Detweiler, J. L. White, S. L. Bernasek, A. B. Bocarsly, *Langmuir* **2014**, *30*, 7593–7600.
- [31] B. Hinnemann, P. G. Moses, J. Bonde, K. P. Jørgensen, J. H. Nielsen, S. Horch, I. Chorkendorff, J. K. Nørskov, *J. Am. Chem. Soc.* **2005**, *127*, 5308–5309.
- [32] Y. Abghoui, E. Skúlason, *J. Phys. Chem. C* **2017**, *121*, 24036–24045.
- [33] T. Maeda, T. Takeichi, T. Wada, *Phys. Status Solidi A* **2006**, *203*, 2634–2638.
- [34] R. Zhang, X. Wen, F. Xu, Q. Zhang, L. Sun, *J. Phys. Chem. C* **2020**, *124*, 11922–11929.
- [35] S. Siebentritt, L. Gütay, D. Regesch, Y. Aida, V. Deprédurand, *Sol. Energy Mater. Sol. Cells* **2013**, *119*, 18–25.

Manuscript received: July 6, 2021

Revised manuscript received: August 6, 2021

Accepted manuscript online: August 24, 2021

Version of record online: October 1, 2021